

From Knots to Crystals: Machine-Learned Potentials for Self-Assembling Topological Solitons in Liquid Crystals

Arunkumar Bupathy,^{1,*} Darian Hall,^{2,3} Ivan I. Smalyukh,^{1,2,4,5,†} Gerardo Campos-Villalobos,^{6,7} Rodolfo Subert,⁶ and Marjolein Dijkstra^{6,1,‡}

¹*International Institute for Sustainability with Knotted Chiral Meta Matter (WPI-SKCM²), Hiroshima University, 1-3-1 Kagamiyama, Higashi-Hiroshima, Hiroshima 739-8526, Japan.*

²*Department of Physics, University of Colorado, Boulder, CO 80309, USA*

³*Department of Physics, University of California, Berkeley, CA 94720, USA*

⁴*Department of Electrical, Computer, and Energy Engineering, Materials Science and Engineering Program, University of Colorado, Boulder, CO 80309, USA*

⁵*Renewable and Sustainable Energy Institute, National Renewable Energy Laboratory, University of Colorado, Boulder, CO 80309, USA*

⁶*Soft Condensed Matter and Biophysics, Debye Institute for Nanomaterials Science, Utrecht University, Princetonplein 1, 3584 CC Utrecht, The Netherlands*

⁷*CNR-ISC and Department of Physics, Sapienza University of Rome, p.le A. Moro 2, 00185 Rome, Italy*

(Dated: December 1, 2025)

Knotted fields in classical and quantum systems were long recognized for their non-trivial topologies and particle-like behavior, but practical applications have been limited by the difficulty of stabilizing them. Recently, stable knotted solitonic textures—heliknotons—have been discovered in chiral liquid crystals, forming adaptive crystal assemblies via elastic distortion-mediated interactions. We use machine learning to develop single-site coarse-grained potentials that accurately capture these chiral anisotropic interactions, enabling large-scale simulations beyond the reach of fine-grained methods. Our machine-learned potentials reproduce the experimentally observed assemblies and provide an efficient framework for modeling a wide range of topological textures.

In the 19th century, Gauss and Kelvin proposed that knots within fields could behave like particles, even representing atoms [1–3]. Although this early model did not describe the actual atoms, it played a pivotal role in the emergence of mathematical knot theory. Skyrme and others extended this perspective by modeling subatomic particles as topological solitons [2–4], while knotted field structures also emerged in classical and quantum field theories, fluid mechanics, particle physics, and cosmology [2–11]. Singular vortex lines and topological solitons were identified as particle-like building blocks in superconductors, magnets, and liquid crystals [12–14]. Yet these knotted structures were long considered as isolated objects rather than particle-like building blocks able to self-assemble into extended crystals [7–9, 15–18], necessary for them to behave as ordered metamatter.

Chiral liquid crystals (CLC) host a multitude of topological structures, including skyrmions, torons, hopfions and möbiusons, stabilized by the medium’s chirality [19–28]. Notably, heliclotons—Hopf solitons in a helical background, or equivalently vortex knots in the immaterial helical axis field—exhibit particle-like behavior, including Brownian motion and hierarchical self-organization into crystals [26, 27], overcoming the barrier to form ordered solitonic metamatter. Unlike atomic, molecular, or colloidal crystals, the symmetry of heliknoton lattices can be tuned by small experimental adjustments [26, 27, 29], making them promising for information storage, computing, light modulation, and photonics. Understanding how such assemblies emerge and adapt to perturbations naturally raises the question of

what effective forces govern heliknoton interactions.

The forces at play manifest as strongly anisotropic interactions, with pair potentials tunable from attractive to repulsive, spanning tens to thousands of $k_B T$, arising from long-range perturbations of the surrounding helical fields [26]. Although these broad features are well established, the design principles of how to use these effective interactions to control resulting collective behavior remain elusive. Modeling these systems is challenging because the solitons are highly sensitive to small variations in material constants, applied fields, geometry, and boundary conditions. Previous studies have primarily relied on fine-grained simulations [26, 27] and collective-variable models to describe the dynamics of individual solitonic objects [30–32]. Particle-like descriptions are appealing as they provide a tractable framework for studying collective phenomena. Existing approaches include iterative Boltzmann inversion [33] or simplified models based on exponentials, Gaussians [34, 35], or elastic multipoles [36]. While these methods capture the qualitative aspects of soliton dynamics and interactions, they either assume rigid textures, limiting accuracy, or generalize poorly to anisotropic or chiral interactions.

In this Letter, we employ a machine learning (ML) approach to develop effective coarse-grained potentials for modeling solitonic interactions and self-assembly, using heliclotons in CLCs as a prototype. Our results demonstrate that heliclotons behave as quasiparticles that self-organize into complex crystals, while also enabling large-scale simulations of interacting solitons to accelerate the design and discovery of knotted metamatter.

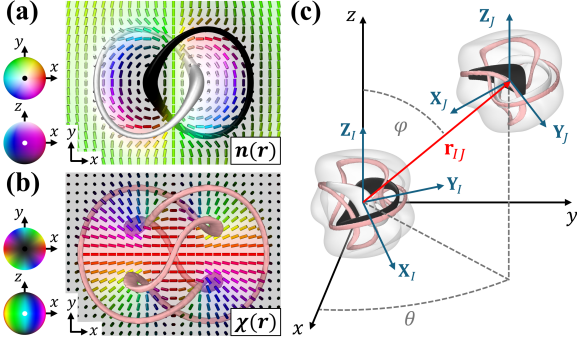


FIG. 1. Cross-sections through the horizontal mid-plane showing (a) the heliknoton's director field $\mathbf{n}(\mathbf{r})$ and (b) the helical field $\chi(\mathbf{r})$. Non-polar $\mathbf{n}(\mathbf{r})$ admits a smooth vectorization while remaining nonsingular, as depicted using a color scheme based on two-sphere order parameter space of vectorized $\mathbf{n}(\mathbf{r})$. Linked loops in (a) are preimages of vertical orientations in smoothly vectorized $\mathbf{n}(\mathbf{r})$, and the light red tube in (b) shows the singular regions in nonpolar $\chi(\mathbf{r})$ forming a trefoil knot; a colored sphere with diametrically opposite points identified decodes orientations of $\chi(\mathbf{r})$. (c) Schematic illustrating the position and orientation coordinates used in the coarse-grained model of heliknoton-pair interactions. The gray isosurfaces surrounding the preimages and vortex knots highlight localized regions where $\chi(\mathbf{r})$ exhibits significant deviations from its uniform far-field background.

Our approach begins by computing interaction energies for a set of heliknoton pair configurations, which serve as the training data for the coarse-grained (CG) model. These energies are obtained from fine-grained (FG) simulations based on the Frank-Oseen free-energy functional, which describes the energetic cost of spatial deformations in the nematic director field $\mathbf{n}(\mathbf{r})$ when heliknotons are embedded in a helicoidal background with cholesteric pitch length p and confined within a slab of thickness d . Figs. 1(a,b) show the director field $\mathbf{n}(\mathbf{r})$ and the helical axis field $\chi(\mathbf{r})$, which represents the local twist axis of the director field for an elementary heliknoton. The linked loops in (a) correspond to the preimages of vertical orientations in $\mathbf{n}(\mathbf{r})$, while the light red tube in (b) shows the singular regions of $\chi(\mathbf{r})$ that form a trefoil knot. We initialize a heliknoton pair (I, J) at a prescribed separation vector $\mathbf{r}_{IJ} = (\Delta x, \Delta y, \Delta z)$ as shown in Fig. 1(c), and subsequently minimize the free energy to determine the corresponding pair interaction energy $\Delta F(\mathbf{r}_{IJ})$. The elastic constants match those of the experimental liquid crystal (LC-1 and LC-2) mixtures reported in Refs. [26, 37]; see End Matter.

Our CG model treats each heliknoton as an effective particle, with the total energy of the system given by the sum of pairwise interactions. A dimer configuration is characterized by the center-to-center separation $r_{IJ} = |\mathbf{r}_{IJ}|$, and the angular variables $\Omega_i \equiv \Omega_i(\mathbf{X}_i, \mathbf{Y}_i, \mathbf{Z}_i)$, where $\mathbf{X}_i, \mathbf{Y}_i$ and \mathbf{Z}_i are the body-fixed axes representing the orientation of the heliknoton $i \in \{I, J\}$,

as well as $\Omega_{IJ} = (\varphi, \theta)$, describing the orientation of \mathbf{r}_{IJ} . For heliknotons embedded in a CLC with planar anchoring at the top and bottom surfaces, the orientation of heliknoton i is coupled to its vertical position z_i by the helical constraint: $\mathbf{X}_i = (\cos qz_i, \sin qz_i, 0)$, $\mathbf{Y}_i = (-\sin qz_i, \cos qz_i, 0)$ and $\mathbf{Z}_i = (0, 0, 1)$, $q = 2\pi/p$. Following [38], we express the interaction potential as

$$\Phi_{IJ} = \sum_k^{N_s} w_k G_k, \quad (1)$$

where $G_k \equiv G_k(r_{IJ}, \Omega_I, \Omega_J, \Omega_{IJ})$ are symmetry functions characterizing the local environment of the interacting particles, w_k are the expansion coefficients, and N_s is the number of terms, chosen to achieve the desired accuracy. The symmetry functions are factorized as $G_k = \Lambda_k(r_{IJ})\Psi_k(\Omega_I, \Omega_J, \Omega_{IJ})f_c(r_{IJ})$, where $\Lambda(r_{IJ})$ and $\Psi(\Omega_I, \Omega_J, \Omega_{IJ})$ encode the radial and orientational dependencies, respectively, and $f_c(r_{IJ})$ is a smooth cutoff function. Following Refs. [38–40], we write $\Psi_k(\Omega_I, \Omega_J, \Omega_{IJ}) = \prod_j S_j(\Omega_I, \Omega_J, \Omega_{IJ})^{a_{kj}}$, where $a_{kj} \in \{0, 1, 2, 3, \dots\}$ is an exponent and S_j are from a set of orthogonal functions known as S -functions. For *achiral* interactions with spatial inversion symmetry, only the first 15 lowest-rank *even* S -functions are required. These correspond to the cosines of the angles between the orientation vectors $\{\mathbf{X}_I, \mathbf{Y}_I, \mathbf{Z}_I\}$, $\{\mathbf{X}_J, \mathbf{Y}_J, \mathbf{Z}_J\}$, and $\hat{\mathbf{r}}_{IJ} = \mathbf{r}_{IJ}/r_{IJ}$. Chiral interactions require another 9 lowest-rank *odd* S -functions that involve cross-products of these vectors. We define the radial part $\Lambda_k(r_{IJ}) = \exp[-\eta_k(r_{IJ} - R_k)^2]$ and the cutoff $f_c(r_{IJ}) = [\cos(\pi r_{IJ}/r_c) + 1]/2$ for $r_{IJ} \leq r_c$, and zero otherwise [41]. Here η_k and R_k are tunable parameters, and r_c is the cutoff distance for the interactions. We generate a large pool of candidate symmetry functions by varying η , R , and a_j over a suitable range of values. The CG potential is constructed by iteratively adding the symmetry function with the largest correlation to Eq. (1) until the desired accuracy is achieved. Full details of the implementation are provided in Refs. [38, 42].

We validate our ML model on thin LC cells, where heliknotons are effectively localized near the horizontal mid-plane for cell thicknesses $d < 3p$ and large electric fields [26]. In this case, the heliknoton pair interactions are only a function of their in-plane separation $\Delta x, \Delta y$, as they share a common orientation. Fig. 2(a) shows the two-dimensional pair interaction potential of heliknotons in the LC-1 mixture, for cell thickness $d = 3p$ and applied voltage $U = 1.9V$. At separations $r > 5p$, the interactions decay to zero. Fig. 2(b) shows the radial profiles of the interaction potential along different $\theta = \tan^{-1}(\Delta y/\Delta x)$. The CG model (lines) accurately reproduces the anisotropic FG interaction potential (symbols), with a root-mean-squared error (RMSE) of $3.9k_B T$ ($T = 293K$), much smaller than the total interaction-strength range ($\sim 6000k_B T$). With the trained CG po-

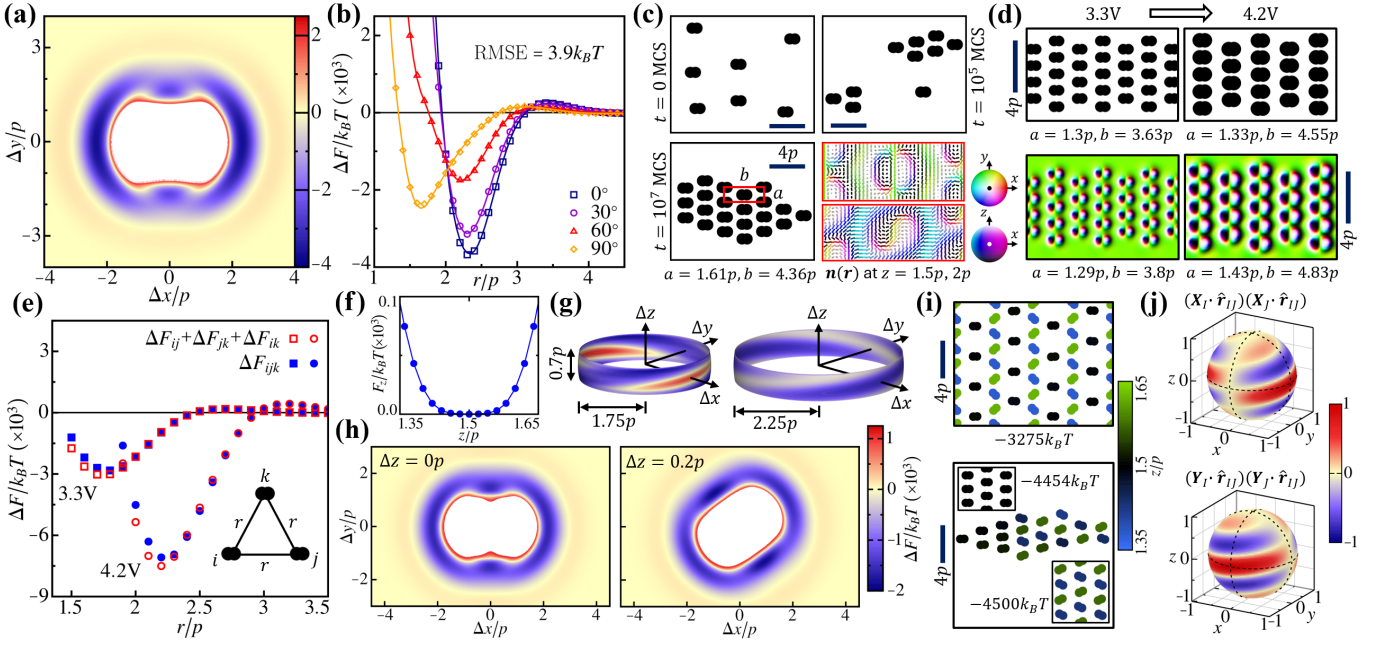


FIG. 2. (a–c) Results for LC-1, $d = 3p$, $U = 2.2V$: (a) Pair interaction potential of heliknotons localized on the horizontal mid-plane of the LC cell, from fine-grained (FG) simulations, shown as a color map. (b) Radial profiles of the FG pair potential (symbols) compared with the coarse-grained (CG) model (lines), along different $\theta = \tan^{-1}(\Delta y/\Delta x)$. (c) Heliknoton assemblies at successive stages of a Monte Carlo (MC) simulation using the CG model; the black symbols represent heliknoton cores and time is measured in MC sweeps (MCS). The bottom-right panel shows horizontal sections of $\mathbf{n}(\mathbf{r})$ at different heights in a unit cell from FG simulations; the color spheres depict the $\mathbf{n}(\mathbf{r})$ orientations. (d–e) Results for LC-2, $d = 2p$: (d) Electrostriction of a heliknoton crystal obtained from MC (top) and FG (bottom) simulations, following a voltage change from $U = 3.3V$ to $4.2V$. (e) Comparison of three-body energies versus the sum of pairwise energies from FG simulations. (f–i) Results for LC-1, $d = 3p$, $U = 2.08V$: (f) z -dependence of the potential experienced by an individual heliknoton. (g) Three-dimensional heliknoton pair potential shown for separation distances $1.75p$ and $2.25p$, color maps on spherical shells truncated by the sampled vertical range. (h) Horizontal sections of the pair potential at different vertical separations Δz . (i) Snapshots from MC simulations showing the stability of a stretched kagome crystal (top) and self-assembly into rhombic crystals (bottom); colors represent the z -position of the heliknotons. The insets show the two observed rhombic crystals (not unit cells) along with the corresponding energy per heliknoton. (j) The S -function pairs that contribute to the chirality of the CG model, visualized color maps on the unit sphere defined by $\hat{\mathbf{r}}_{IJ}$.

tential, we simulate the self-assembly of heliknotons using Monte Carlo (MC) simulations [43–45]. Fig. 2(c) shows snapshots of the heliknoton assemblies at successive stages of the simulation. The rhombic crystal structure that self-assembled in our simulations, exhibiting a centered rectangular unit cell, closely matches the experimental observations [26, 46]. Although the lattice is rectangular, the crystal inherits the chirality of the heliknoton textures as seen from the bottom right panels of Fig. 2(c) showing horizontal sections of $\mathbf{n}(\mathbf{r})$, from FG simulations of a unit cell.

Subsequently, we test our ML approach to capture small changes in experimental conditions by training the models on data from FG simulations in the LC-2 mixture ($d = 2p$) at electric field strengths of $3.3V$ and $4.2V$. We first perform MC simulations using the CG potential at $3.3V$, to identify the crystal lattice self-assembled by the heliknotons. Initializing a crystallite in this state (top left, Fig. 2(d)), we then switch the interaction potential to that at $4.2V$ and observe its expansion (top

right, Fig. 2(d)). FG simulations using the Frank–Oseen functional (bottom panels, Fig. 2(d)) yield slightly different lattice constants, likely reflecting the absence of many-body interactions in the CG model. To test this, we compare the three-body energy ΔF_{ijk} of a heliknoton triplet (i, j, k) arranged in an equilateral triangle of length r versus the sum of pairwise energies ΔF_{ij} , ΔF_{jk} , ΔF_{ik} in Fig 2(e). For separations $r > 2.5p$, we observe good agreement between the full three-body potential and the sum of two-body terms. At smaller separations, although the pairwise sum underestimates the total interaction energy, the qualitative behavior is still successfully captured. Nonetheless, the CG simulations are highly efficient, completing in about 2.7 hours on four Intel i9-13900 CPU cores, compared to 28.1 hours for the FG simulations on an Nvidia RTX A4000 GPU.

We next consider the case where heliknotons form a stretched kagome lattice with staggered z -positions (LC-1, $d = 3p$, $U = 2.08V$). In this setting, it is also necessary to sample the energy of a single heliknoton as a

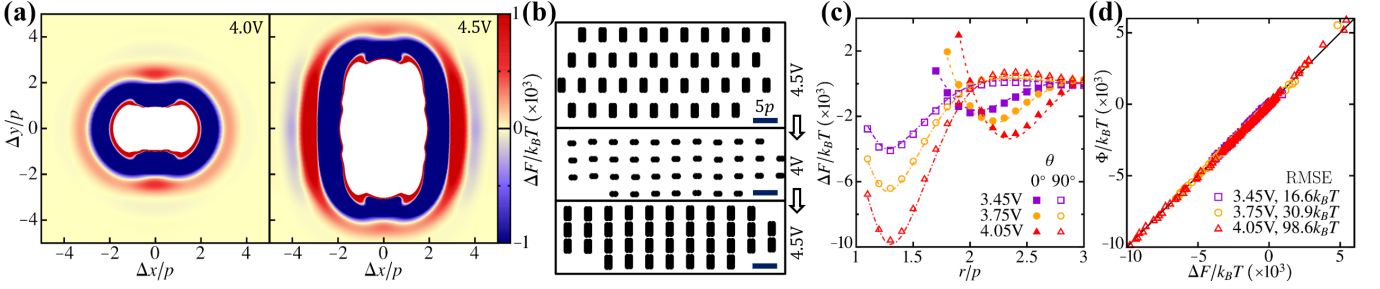


FIG. 3. Results for LC-2, $d = 2p$: (a) Two-dimensional heliknoton pair potentials at voltages $U = 4V$ and $4.5V$ shown as color maps. (b) Heliknoton assemblies from MC simulations using the CG models, as the voltage is cycled from $4.5V$ to $4V$ and back. (c) Interpolated heliknoton pair potentials (dotted dashed lines) compared with those from FG simulations (symbols) at different applied voltages. (d) Parity plots comparing the interpolated potentials (Φ) versus the ground truth from the FG simulations (ΔF) along with the RMS errors.

function of its z -position, since individual heliknotons interact with the LC cell surfaces. The z -potential shown in Fig. 2(f) exhibits a shallow minimum around the vertical midsection ($1.5p$) of the cell. Fig. 2(g) shows the three-dimensional heliknoton pair potential for separation distances $1.75p$ and $2.25p$, as color maps on spherical shells truncated by the sampled vertical range, whereas Fig. 2(h) presents the corresponding horizontal sections of the potential at different vertical separations Δz . The twist observed in Figs. 2(g,h) clearly shows that the interactions are not only anisotropic but also chiral. Although the trained CG model showed a slightly higher RMSE of $6.4k_B T$, this is small compared to the total interaction range ($\sim 3000k_B T$). MC simulations using the CG model confirm the stability of the stretched kagome crystal with staggered z -positions (top panel, Fig. 2(i)), as observed experimentally [26, 46], when initialized in this configuration. The opposite-handed configuration, with the z -positions swapped, is higher in energy by about $330k_B T$ and unstable. Self-assembly from a dilute gas, however, produces rhombic crystals, with the heliknotons either near the horizontal mid-plane or adopting staggered z -positions (bottom panel, Fig. 2(i)), the latter being lowest in energy. Interestingly, inspection reveals that the model contains the S -function (dot-product) pairs $(\mathbf{X}_I \cdot \hat{\mathbf{r}}_{IJ})(\mathbf{X}_J \cdot \hat{\mathbf{r}}_{IJ})$ and $(\mathbf{Y}_I \cdot \hat{\mathbf{r}}_{IJ})(\mathbf{Y}_J \cdot \hat{\mathbf{r}}_{IJ})$, which, although achiral by themselves, inherit chirality due to the coupling of $\mathbf{X}_{I,J}$ and $\mathbf{Y}_{I,J}$ with the helical background (Fig. 2(j)), via a sinusoidal (odd) contribution in the vertical separation of heliknotons; see End Matter.

To demonstrate how the ML-based CG model improves search efficiency, we present an example where a simple cycling of the applied voltage reconfigures a heliknoton assembly. Fig. 3(a) shows the two-dimensional pair potential of heliknotons in LC-2, for cell thickness $d = 2p$ at applied voltages $U = 4V$ and $4.5V$. We observe a substantial change in the anisotropy of the interactions, with increased energy barriers. When allowed to self-assemble at $4.5V$ the heliknotons form a rhombic crystal (top panel, Fig. 3(b)). Cycling the voltage from $4.5V$ and down to

$4V$ and back drives the heliknotons into a stable rectangular lattice (middle and bottom panels, Fig. 3(b)).

Crucially, our method is not limited to the discrete voltages at which the CG models are trained, but allows interpolation across voltages. Given the CG potentials trained at a set of voltages $\{U_i\}$, represented as $\Phi_i = \sum_k w_{ki}^0 G_{ki}$ with w_{ki}^0 and G_{ki} being the coefficients and symmetry functions at U_i , we can construct a voltage dependent model: $\Phi(U) = \sum_{k,i} w_{ki}(U) G_{ki}$. The voltage-dependent weights $w_{ki}(U)$ satisfy $w_{ki}(U_i) = w_{ki}^0$ and may be interpolated using simple methods, provided the U_i are not too far apart. As an example, using cubic spline for the $w_{ki}(U)$, we interpolate the interaction potentials at $3.45V$, $3.75V$ and $4.05V$ from CG models trained at $3.3V$, $3.6V$, $3.9V$ and $4.2V$, for LC-2 cells of thickness $d = 2p$. As seen in Fig. 3(c), the resulting interpolated potentials (dotted dashed lines) accurately capture the radial and angular dependence of the interactions from FG simulations (symbols) across the interpolation range. Fig. 3(d) compares the interpolated potentials (Φ) against the ground-truth (ΔF) obtained from the FG simulations. The RMS errors range from about $17k_B T$ to $100k_B T$, and are relatively small compared to the scale of interactions $\sim 10^4 k_B T$. This could also be extended to include material constants, enabling efficient exploration of the broader parameter space without retraining the CG potentials.

In summary, our work establishes a general framework for modeling topological solitons as quasiparticles described solely by their geometric centers and orientations. By constructing machine-learned coarse-grained potentials, we demonstrated the self-assembly of heliknotons into complex closed and open crystal lattices, in qualitative agreement with experiments. This approach enables large-scale simulations at a fraction of the computational cost of fine-grained methods. Although our focus has been on chiral liquid crystals, our method is broadly applicable to particle-like topological textures, enabling the exploration of emergent collective phenomena across diverse soft and hard condensed matter systems.

A.B. acknowledges the N8 Centre of Excellence in Computationally Intensive Research (N8 CIR) funded by the N8 research partnership and EPSRC (Grant No. EP/T022167/1), coordinated by the Universities of Durham, Manchester and York, for access to computational resources. I.I.S. and D.H. acknowledge the support by the U.S. Department of Energy, Office of Basic Energy Sciences, Division of Materials Sciences and Engineering, under contract DE-SC0019293 with the University of Colorado at Boulder.

* abupathy@hiroshima-u.ac.jp

† ivan.smalyukh@colorado.edu

‡ m.dijkstra@uu.nl

- [1] L. H. Kauffman, *Knots and Physics* (World Scientific, 2001).
- [2] N. Manton and P. Sutcliffe, *Topological Solitons* (Cambridge University Press, 2004).
- [3] Y. M. Shnir, *Topological and Non-Topological Solitons in Scalar Field Theories* (Cambridge University Press, 2018).
- [4] T. H. R. Skyrme, A non-linear field theory, Proceedings of the Royal Society of London. Series A. Mathematical and Physical Sciences **260**, 127 (1961).
- [5] J.-S. B. Tai, P. J. Ackerman, and I. I. Smalyukh, Topological transformations of Hopf solitons in chiral ferromagnets and liquid crystals, Proceedings of the National Academy of Sciences **115**, 921 (2018).
- [6] L. Faddeev and A. J. Niemi, Stable knot-like structures in classical field theory, Nature **387**, 58 (1997).
- [7] H. K. Moffatt and R. L. Ricca, Helicity and the Călugăreanu invariant, Proceedings of the Royal Society of London. Series A: Mathematical and Physical Sciences **439**, 411 (1992).
- [8] M. W. Scheeler, W. M. van Rees, H. Kedia, D. Kleckner, and W. T. Irvine, Complete measurement of helicity and its dynamics in vortex tubes, Science **357**, 487 (2017).
- [9] D. Kleckner and W. T. Irvine, Creation and dynamics of knotted vortices, Nature Physics **9**, 253 (2013).
- [10] R. V. Buniy, J. Cantarella, T. W. Kephart, and E. J. Rawdon, Tight knot spectrum in QCD, Physical Review D **89**, 054513 (2014).
- [11] R. Shankar, Applications of topology to the study of ordered systems, Journal de Physique **38**, 1405 (1977).
- [12] P. M. Chaikin and T. C. Lubensky, *Principles of Condensed Matter Physics* (Cambridge University Press, 1995).
- [13] J. H. Han, *Skyrmions in Condensed Matter* (Springer, 2017).
- [14] D. Foster, C. Kind, P. J. Ackerman, J.-S. B. Tai, M. R. Dennis, and I. I. Smalyukh, Two-dimensional skyrmion bags in liquid crystals and ferromagnets, Nature Physics **15**, 655 (2019).
- [15] Y. Bouligand, Recherches sur les textures des états mésomorphes. 6—dislocations coins et signification des cloisons de grandjean-cano dans les cholestériques, Journal de Physique **35**, 959 (1974).
- [16] Y. Bouligand, B. Derrida, V. Poenaru, Y. Pomeau, and G. Toulouse, Distortions with double topological character: the case of cholesterics, Journal de Physique **39**, 863 (1978).
- [17] T. Machon and G. P. Alexander, Knotted defects in nematic liquid crystals, Physical Review Letters **113**, 027801 (2014).
- [18] J.-S. B. Tai, J.-S. Wu, and I. I. Smalyukh, Geometric transformation and three-dimensional hopping of hopf solitons, Nat. Commun. **13**, 2986 (2022).
- [19] I. I. Smalyukh, Y. Lansac, N. A. Clark, and R. P. Trivedi, Three-dimensional structure and multistable optical switching of triple-twisted particle-like excitations in anisotropic fluids, Nature Materials **9**, 139 (2010).
- [20] J.-I. Fukuda and S. Žumer, Quasi-two-dimensional Skyrmion lattices in a chiral nematic liquid crystal, Nature Communications **2**, 246 (2011).
- [21] P. J. Ackerman, R. P. Trivedi, B. Senyuk, J. van de Lagemaat, and I. I. Smalyukh, Two-dimensional skyrmions and other solitonic structures in confinement-frustrated chiral nematics, Physical Review E **90**, 012505 (2014).
- [22] D. Seč, S. Čopar, and S. Žumer, Topological zoo of free-standing knots in confined chiral nematic fluids, Nature Communications **5**, 3057 (2014).
- [23] Y. Guo, S. Afghah, J. Xiang, O. D. Lavrentovich, R. L. B. Selinger, and Q.-H. Wei, Cholesteric liquid crystals in rectangular microchannels: skyrmions and stripes, Soft Matter **12**, 6312 (2016).
- [24] G. Posnjak, S. Čopar, and I. Mušević, Points, skyrmions and torons in chiral nematic droplets, Scientific Reports **6**, 26361 (2016).
- [25] P. J. Ackerman and I. I. Smalyukh, Static three-dimensional topological solitons in fluid chiral ferromagnets and colloids, Nature Materials **16**, 426 (2017).
- [26] J.-S. B. Tai and I. I. Smalyukh, Three-dimensional crystals of adaptive knots, Science **365**, 1449 (2019).
- [27] R. Voinescu, J.-S. B. Tai, and I. I. Smalyukh, Hopf Solitons in Helical and Conical Backgrounds of Chiral Magnetic Solids, Physical Review Letters **125**, 057201 (2020).
- [28] H. Zhao, J.-S. B. Tai, J.-S. Wu, and I. I. Smalyukh, Liquid crystal defect structures with Möbius strip topology, Nature Physics **19**, 451 (2023).
- [29] D. Hall, J.-S. B. Tai, L. H. Kauffman, and I. I. Smalyukh, Fusion and fission of particle-like chiral nematic vortex knots, Nature Physics 10.1038/s41567-025-03107-0 (2025).
- [30] C. Long and J. V. Selinger, Coarse-grained theory for motion of solitons and skyrmions in liquid crystals, Soft Matter **17**, 10437 (2021).
- [31] T. Alvim, M. M. T. d. Gama, and M. Tasinkevych, Collective variable model for the dynamics of liquid crystal skyrmions, Communications Physics **7**, 2 (2024).
- [32] A. W. Teixeira, M. Tasinkevych, and C. S. Dias, Particle-based model of liquid crystal skyrmion dynamics, Soft Matter **20**, 2088 (2024).
- [33] Y. Ge, J. Rothörl, M. A. Brems, N. Kerber, R. Gruber, T. Dohi, M. Kläui, and P. Virnau, Constructing coarse-grained skyrmion potentials from experimental data with Iterative Boltzmann Inversion, Communications Physics **6**, 30 (2023).
- [34] S.-Z. Lin, C. Reichhardt, C. D. Batista, and A. Saxena, Particle model for skyrmions in metallic chiral magnets: Dynamics, pinning, and creep, Physical Review B **87**, 214419 (2013).
- [35] L. González-Gómez, J. Castell-Queralt, N. Del-Valle, A. Sanchez, and C. Navau, Analytical modeling of the in-

- teraction between skyrmions and extended defects, Physical Review B **100**, 054440 (2019).
- [36] A. W. Teixeira, C. S. Dias, and M. Tasinkevych, Liquid crystal skyrmions as elastic multipoles (2024), arXiv:2410.03967 [cond-mat.soft].
- [37] J.-S. B. Tai and I. I. Smalyukh, Surface anchoring as a control parameter for stabilizing torons, skyrmions, twisted walls, fingers, and their hybrids in chiral nematics, Physical Review E **101**, 042702 (2020).
- [38] G. Campos-Villalobos, R. Subert, G. Giunta, and M. Dijkstra, Machine-learned coarse-grained potentials for particles with anisotropic shapes and interactions, npj Computational Materials **10**, 228 (2024).
- [39] L. Blum and A. J. Torruella, Invariant Expansion for Two-Body Correlations: Thermodynamic Functions, Scattering, and the Ornstein—Zernike Equation, The Journal of Chemical Physics **56**, 303 (1972).
- [40] A. Stone, The description of bimolecular potentials, forces and torques: the S and V function expansions, Molecular Physics **36**, 241 (1978).
- [41] J. Behler and M. Parrinello, Generalized Neural-Network Representation of High-Dimensional Potential-Energy Surfaces, Physical Review Letters **98**, 146401 (2007).
- [42] G. Campos-Villalobos, E. Boattini, L. Filion, and M. Dijkstra, Machine learning many-body potentials for colloidal systems, The Journal of Chemical Physics **155**, 174902 (2021).
- [43] S. Whitelam and P. L. Geissler, Avoiding unphysical kinetic traps in Monte Carlo simulations of strongly attractive particles, The Journal of Chemical Physics **127**, 154101 (2007).
- [44] S. Whitelam, E. H. Feng, M. F. Hagan, and P. L. Geissler, The role of collective motion in examples of coarsening and self-assembly, Soft Matter **5**, 1251 (2009).
- [45] L. O. Hedges, LibVMMC.
- [46] Despite simplifications used in the Frank-Oseen free-energy calculations, the simulations faithfully capture the experimental trends, with a difference of only about 0.3V.
- [47] Rapini, A. and Papoular, M., Distorsion d'une lamelle nématique sous champ magnétique conditions d'ancrage aux parois, J. Phys. Colloques **30**, C4 (1969).
- [48] V. M. Kuchkin, N. S. Kiselev, F. N. Rybakov, I. S. Lobanov, S. Blügel, and V. M. Uzdin, Heliknoton in a film of cubic chiral magnet, Frontiers in Physics **11**, 1201018 (2023).

END MATTER

Frank-Oseen free energy calculations

The interaction energies of heliknoton pairs are obtained from fine-grained simulations based on the Frank-Oseen free-energy functional, which describes the energetic cost of spatial deformations of the nematic director

Mixture	K_{11} (pN)	K_{22} (pN)	K_{33} (pN)	$\Delta\epsilon$
LC-1	6.4	3	10	13.8
LC-2	14.1	6.7	15.5	3.4

TABLE I. Material parameters of the LC mixtures used in the Frank-Oseen calculations.

field $\mathbf{n}(\mathbf{r})$:

$$F_{\text{bulk}} = \int d^3r \left\{ \frac{K_{11}}{2} (\nabla \cdot \mathbf{n})^2 + \frac{K_{22}}{2} \left[\mathbf{n} \cdot (\nabla \times \mathbf{n}) + \frac{2\pi}{p} \right]^2 + \frac{K_{33}}{2} [\mathbf{n} \times (\nabla \times \mathbf{n})]^2 - \frac{\epsilon_0 \Delta\epsilon}{2} (\mathbf{E} \cdot \mathbf{n})^2 \right\}, \quad (2)$$

where K_{11} , K_{22} and K_{33} are the Frank elastic moduli associated with splay, twist, and bend deformations, respectively, p is the cholesteric pitch, ϵ_0 is the vacuum permittivity, and $\Delta\epsilon$ is the dielectric anisotropy. We do not include the contribution of splay-bend deformations, as it was shown to have little effect on heliknoton stability [26].

The surface anchoring energy follows the Rapini-Papoular form [47]:

$$F_{\text{surface}} = - \int d^2r \frac{W}{2} (\mathbf{n} \cdot \mathbf{n}_0)^2, \quad (3)$$

where W is the anchoring strength and $\mathbf{n}_0 = \mathbf{y}$ is the easy axis, corresponding to unidirectional planar anchoring. We employ periodic boundary conditions along the x and y directions.

The free-energy functional is numerically minimized using a variational relaxation routine employing second-order finite differences. At each step $\mathbf{n}(\mathbf{r})$ is updated as $n_i^{\text{new}} = n_i^{\text{old}} - \alpha \Delta t [F]_{n_i}$, where $[F]_{n_i}$ is the functional derivative of F with respect to the component n_i [37], and $\Delta t = \Delta h^2 / [2 \max(K)]$ is the maximum stable time step, where Δh is the computational grid spacing and $\max(K)$ is the largest elastic constant [25], and $0 \leq \alpha \leq 1$ is a reduced relaxation rate. $\mathbf{n}(\mathbf{r})$ is normalized after each update.

We initialize a pair of heliknotons (I, J) at a prescribed separation vector $\mathbf{r}_{IJ} = (\Delta x, \Delta y, \Delta z)$, followed by numerical minimization of the free energy. The pair interaction potential is then computed as

$$\Delta F = F_2 - 2F_1 + F_0, \quad (4)$$

where F_2 is the free energy (FE) of the relaxed dimer configuration, F_1 is the free energy of a single isolated heliknoton, and F_0 is the free energy of the uniform cholesteric state. Simulations were performed for the liquid crystal mixtures LC-1 and LC-2 studied in Ref. [26], with the material parameters listed in Table. I, and with helical pitch $p = 5\mu\text{m}$ and surface anchoring strength $W = 10^{-4} \text{ J/m}^2$.

In our simulations, both the external field \mathbf{E} and the far-field helical axis χ_0 were aligned along the z -direction and non-local field effects were excluded. The simulation volume was discretized into a computational grid with 32 points per pitch p , per axis. The x and y dimensions of the simulation cell were taken sufficiently large ($L \geq 12p$) to minimize interactions with the periodic images. For a given set of parameters, a single heliknoton is first generated using an ansatz [29, 48] and relaxed for 64000 steps at a relaxation rate $\alpha = 0.35$. This *pre-relaxed* ansatz is then used to initialize the pair configurations which were subsequently relaxed for a further 2000 steps to obtain the pair potential. For LC-2 at 4.5V, the heliknoton ansatz was pre-relaxed for 64000 steps with a surface anchoring strength $W = 10^{-6}$ J/m² followed by another 16000 steps at $W = 10^{-4}$ J/m², prior to sampling the interaction potential.

Symmetry Functions

The construction of the coarse-grained potentials begins with generating a large but manageable pool of candidate symmetry functions. The candidate pool was obtained by systematically combining values of the parameters η , R , and a_j . Specifically, η was chosen from the set $\{34.6, 6.56, 2.48, 1.24, 0.73, 0.47\}$. For a given η , the set of R values is given by $R = \left[1.1 + \frac{0.1666}{\sqrt{\eta}}i\right]p$, where $i \in \{0, 1, 2, 3, \dots\}$, with the constraint $R < r_c$ ($r_c = 6p$). The

angular basis functions Ψ were constructed as products of the 15 lowest-rank *even* S -functions, raised to positive integer powers a_j , with the constraint $\sum_j a_j \leq a_{\max}$.

In most cases studied here, setting $a_{\max} = 8$ yielded accurate coarse-grained representations of heliknoton pair interactions, using $N_s = 32$ terms selected from the candidate pool, with root-mean-square errors below $10k_B T$. For LC-2 at $U = 4.5$ V, however, convergence required up to 64 terms with $a_{\max} = 16$.

The effective number of candidate functions is substantially reduced by the fact that several of the lowest-rank S -functions vanish or become constants due to the alignment of heliknotons with the helical background. Interestingly, *odd* S -functions were not required, despite the intrinsically chiral nature of the heliknoton textures. In this regard, although the learned heliknoton potentials are constructed from (achiral) dot-product features of the in-plane orientation vectors, such as $(\mathbf{X}_I \cdot \hat{\mathbf{r}}_{IJ})(\mathbf{X}_J \cdot \hat{\mathbf{r}}_{IJ})$ and $(\mathbf{Y}_I \cdot \hat{\mathbf{r}}_{IJ})(\mathbf{Y}_J \cdot \hat{\mathbf{r}}_{IJ})$, the coupling of the heliknoton orientations \mathbf{X}_i and \mathbf{Y}_i ($i \in \{I, J\}$) with the helical background renders these features chiral. Specifically, under the constraints $\mathbf{X}_i = (\cos qz_i, \sin qz_i, 0)$, $\mathbf{Y}_i = (-\sin qz_i, \cos qz_i, 0)$, where z_i is the vertical position of heliknoton i and $q = 2\pi/p$, it can be shown that the angular basis functions mentioned above gain an odd contribution $\propto \sin(q\Delta z)$, which changes sign when heliknoton J is positioned above ($+\Delta z$) versus below ($-\Delta z$) heliknoton I . It also changes sign under a reversal of the handedness ($q \rightarrow -q$) of the helical background. Thus, handed interactions emerge naturally and can be fully captured even without explicitly chiral descriptors.